Mechanical Systems and Signal Processing 200 (2023) 110592

Contents lists available at ScienceDirect

Mechanical Systems and Signal Processing

journal homepage: www.elsevier.com/locate/ymssp

Comprehensive model of a rotating flexible wheelset for high-frequency railway dynamics

Luis Baeza [a,*], Juan Giner-Navarro [a], Christopher Knuth [b], David J. Thompson [b]

[a] Instituto de Ingeniería Mecánica y Biomecánica, Universitat Politècnica de València, Valencia, Spain
[b] Institute of Sound and Vibration Research, University of Southampton, Southampton, UK

ARTICLE INFO

Keywords:
Railway vehicle-track interaction
Railway wheels
Rotors
Lagrangian coordinates
Eulerian coordinates
Instrumented wheelsets
Dynamometric wheelsets
Load-measuring wheelsets

ABSTRACT

The development and application of wheelset models that realistically incorporate both flexibility and rotation, constitutes a topic that has recently been active in the literature regarding high-frequency railway dynamics. The main application of these models is the simulation of the railway vehicle-track dynamic interaction, which justifies the fact that most of them are formulated using coordinates that do not rotate with the solid (Euler coordinates). Wheelset models based on rotating coordinates are scarce, although they have some practical applications when the vibration response at points fixed in the material is required (e.g., to simulate the signal of a transducer that is fixed at a point on the wheelset). The present work provides a global method in the modelling of a flexible and rotating railway wheelset, independent of the coordinates used (fixed or rotating). To achieve this, a compact formulation is developed adopting axisymmetric coordinates through both Lagrangian and Eulerian approaches, which are related by means of a coordinate transformation. The equations of motion that are deduced for both reference frames are linear, which allows the natural frequencies to be obtained as seen from a fixed frame as well as the ones observed for a system that rotates with the wheelset. The relationship between the natural frequencies obtained from both equations of motion is expressed as a closed-form formula that depends on the angular velocity of the wheelset. The model is applied to simulate the response measured by the strain gauges used in load-measuring wheelsets, in which a vertical force is acting in the wheel-rail contact. The results can contribute to establish limits on the use of the instrumented wheelsets based on the angular velocity and the frequency of the force applied in the wheel-rail contact.

1. Introduction

Within the dynamic problems that affect rail transport, those that correspond to the coupled dynamics of a vehicle and the track are of special relevance for the operating costs and the environmental impact. Although this type of study is carried out frequently through wheelset models that are considered rigid, certain problems are potentially sensitive to the effect of the wheelset flexibility and its rotation. This would be the case for studies realised through flexible and rotating wheelsets on rolling noise [1,2], polygonal wear of the wheel tread [3–5], corrugation of rails [6], the response to rail irregularities [7] and the fatigue life of railway axles [8] due to stresses induced by the aforementioned wheel and track imperfections. This interest justifies the special emphasis that researchers have

* Corresponding author at: Edificio 5E, Ing. Mecánica, Universidad Politécnica de Valencia, Camino de Vera, s/n, 46022 Valencia, Spain.
E-mail address: baeza@mcm.upv.es (L. Baeza).

https://doi.org/10.1016/j.ymssp.2023.110592
Received 10 October 2022; Received in revised form 27 April 2023; Accepted 4 July 2023
Available online 12 July 2023

placed in recent years on the development of advanced models for the wheelset, among which most have focused on the use of non-rotating coordinates due to their capability to study the interaction of the wheelset with non-rotating systems, in particular the track. This approach, adopting Euler coordinates, allows the forces that are transmitted from the non-rotating structures to the rotating wheelset (through the wheel-rail contact and the axle boxes) to be applied at fixed spatial points. In turn, non-rotating coordinate models facilitate certain calculations, e.g. acoustic radiation due to the wheel vibration (enabling the use of air-conforming finite element (FE) meshes and boundary element models) and avoid certain problems associated with classical FE models such as the parametric excitation that occurs when a moving load is applied to the three-dimensional mesh (shifting the contact point on the element for each instant).

Following this approach, one of the first developments for the wheelset model is presented in Ref. [9]. Taking advantage of its geometry of revolution, the mode shapes in a non-rotating frame of reference can be used as a basis to represent any displacement of the solid. Similar developments of a rotating wheelset model defined in Eulerian coordinates are presented in [8]. As a step forward in the wheelset modelling, Refs. [10,11] consider the dynamics of the wheelset in curves. To do this, a non-rotating trajectory frame of reference is defined following the geometry of the track. A significant advance in railway wheelset modelling was the use of axisymmetric coordinates [12], which considerably reduces the computational cost associated with the simulation and the numerical calculation of the equation of motion matrices. Although axisymmetric models assume the separation of variables and a truncated Fourier approach, they reduce the numerical errors associated with the FE discretisation in the circumferential direction in most practical cases. The wheel rotation was replaced by a moving load in [13], to calculate the response of a rotating railway wheel from a non-rotating axisymmetric FE model, but excluding gyroscopic and centrifugal effects. Refs. [14–16] present FE models of beam-like and axisymmetric rotors in both rotating and non-rotating coordinates. They were used for the analysis of rotating shafts, or disc-shaft assemblies, that bear similar features to railway wheelsets. In [17] a waveguide FE model was adopted for modelling circular rotating structures and applied to broadband vibration analysis of a rotating tyre. The models in Refs. [14–17] account for the inertial gyroscopic and centrifugal effects induced by the rotation. Geometric stiffening effects like stress stiffening or pre-stress were included in [16,17]. Two axisymmetric models for railway wheelsets based on fixed coordinates have recently been published, differing in terms of the principles of dynamics on which they are based (D'Alembert's principle [18] or Euler–Lagrange equations [19]).

Lagrangian models, which describe the motion through a reference frame that rotates with the solid, are more scarce even though they are able to provide more information about the basic nature of the wheelset vibration. These models are also more suitable when the vibration response is required at material points of the wheelset, for example, when calculating the signal measured by a transducer that is fixed to the wheelset. One practical example of these measurements corresponds to so-called instrumented, or load-measuring, wheelsets, which are used in the homologation tests of railway vehicles following the UIC 518 leaflet [20]. Instrumented wheelsets are conventional ones that are instrumented with strain gauges at points on the wheel web and/or the wheelset axle. Through the signals of the different Wheatstone bridges, the position of the wheel-rail contact point, the vertical force Q and the lateral force Y are obtained. The UIC 518 leaflet establishes various limit values through quantities derived from Y and Q forces, such as the Nadal single-wheel Y/Q limit criterion [21]. To estimate the UIC 518 limits, it is sufficient to measure the signal content below a fairly low frequency limit (depending on the magnitude, below 20 Hz). However, some manufacturers of instrumented wheelsets claim to be able to measure contact forces in a range up to 3 kHz; measuring the force in the contact at such a high frequency would allow monitoring of the railway track. It should be noted that an instrumented wheelset is essentially a load cell, and standard load cells measure below their first natural frequency. Refs. [22,23] develop methodologies to measure vertical wheel-rail contact forces using instrumented wheelsets that includes a compensation for the frequency response of the wheelset to extend the range to 2 kHz. However, neither these nor other related works include the effects associated with the rotation.

In order to overcome the boundary between rotating and non-rotating coordinates approaches, this paper aims to provide a comprehensive modelling approach for the rotating railway wheelset by means of axisymmetric coordinates. No damping is introduced in the model since its value is mostly much smaller than 1% for conventional wheelsets. This modelling approach is independent of the type of reference system adopted, which can also help to facilitate understanding of the phenomena underlying the coupling between the vibration response of a solid and its rotation. To do this, two kinematic formulations, in fixed and rotating axes, respectively, are presented in Section 2. In Section 3.1 the equation of motion in rotating axes (Lagrangian model) is derived, from which the expression in fixed axes (Eulerian model) is derived in Section 3.2 by means of the transformation between coordinates justified in Section 2. Results are presented in Section 4 to illustrate the effects of rotation on wheelset dynamics. With this in mind, the influence of rotational speed on the natural frequencies of the wheelset observed in rotating and non-rotating axes, and the relationship between them, are obtained and analysed. Next, the proposed method is applied to calculate the wheel-rail contact force measured through instrumented wheelsets. This study considers the influence of the angular velocity and the frequency of the wheel-rail contact force. The findings offer new insights into the precision of instrumented wheelsets when vehicles operate at high speeds, and the nature of measurements taken through these devices when the bandwidth is expanded to several kilohertz. These advancements will enhance the accuracy of measurements during very high-speed train homologation tests and aid in the development of track monitoring methods using instrumented wheelsets.

2. Kinematic model of the flexible rotating wheelset

The kinematics of the rotating wheelset are first formulated through a Lagrangian approach making use of a reference frame **xyz** rotating with the solid, in which the **z**-axis is the axis of revolution of the solid. Intrinsic coordinates are used for defining the displacement $\mathbf{p} = \{p_1, p_2, p_3\}^{\mathrm{T}}$ of a material particle of the wheelset depicted in Fig. 1. The position of the particle in the undeformed

configuration of the solid is defined by $\mathbf{u} = \{r, 0, z\}^{\mathrm{T}}$ and the angle θ. The absolute velocity of the particle can be deduced as

$$\mathbf{v} = \Omega \mathbf{J}(\mathbf{u} + \mathbf{p}) + \dot{\mathbf{p}}, \tag{1}$$

where Ω is the constant angular velocity of the wheelset, and

$$J = \begin{bmatrix} 0 & -1 & 0 \\ 1 & 0 & 0 \\ 0 & 0 & 0 \end{bmatrix}. \tag{2}$$

By separation of variables, the displacements due to the deformations of the axisymmetric solid can be expressed through a Fourier series:

$$\mathbf{p}(r, z, \theta) = \sum_{h=0}^{H} \widetilde{\mathbf{p}}_h(r, z)\ \cos\theta h + \sum_{h=1}^{H} \overline{\mathbf{p}}_h(r, \mathrm{z})\ \sin\theta h, \tag{3}$$

h being the harmonic index or the number of nodal diameters, H the number of spatial harmonics considered, and $\widetilde{p}_h$ and $\overline{p}_h$ the amplitudes of each harmonic.

Considering Euler coordinates now, let $\mathbf{w}$ be the displacement of a particle that is in its undeformed configuration in the angular position with respect to the non-rotating frame $\mathbf{x}_0\mathbf{y}_0\mathbf{z}$ given by angle φ. Assuming separation of variables, the dependence of the displacement due to the deformation on the angle φ can be written through a Fourier series as

$$\mathbf{w}(r, z, \varphi) = \sum_{h=0}^{H} \widetilde{\mathbf{w}}_h(r, z)\cos\varphi h + \sum_{h=1}^{H} \overline{\mathbf{w}}_h(r, z)\sin\varphi h. \tag{4}$$

By imposing the condition that the Eulerian and Lagrangian displacements coincide at a certain time instant, then the following relationship is obtained

$$\mathbf{p}(r, z, \theta) = \mathbf{w}(r, z, \Omega t + \theta), \tag{5}$$

and from the Fourier series defined in Eqs. (3) and (4)

$$\sum_{h=0}^{H} \widetilde{\mathbf{p}}_h\cos\theta h + \sum_{h=1}^{H} \overline{\mathbf{p}}_h\sin\theta h = \sum_{h=0}^{H} \widetilde{\mathbf{w}}_h\cos(\Omega h t + \theta h) + \sum_{h=1}^{H} \overline{\mathbf{w}}_h\sin(\Omega h t + \theta h). \tag{6}$$

By first multiplying both terms of the last equation by $\cos\varphi h$ and then integrating with respect to θ between 0 and 2π (and secondly following an analogue procedure multiplying by $\sin\varphi h$), the following equations are obtained

$$\widetilde{\mathbf{p}}_h = \widetilde{\mathbf{w}}_h\cos\Omega h t + \overline{\mathbf{w}}_h\ \sin\Omega h t, \tag{7}$$

$$\overline{\mathbf{p}}_h = -\widetilde{\mathbf{w}}_h\sin\Omega h t + \overline{\mathbf{w}}_h\cos\Omega h t, \tag{8}$$

formulae that correspond to a transformation from Euler to Lagrange coordinates.

3. Equations of motion

3.1. Lagrangian approach

From the particle velocity expression in Eq. (1), the kinetic energy of the system can be expressed as

$$T = \frac{1}{2}\Omega^2 \iiint_V r\rho(\mathbf{u} + \mathbf{p})^{\mathrm{T}}\mathbf{E}(\mathbf{u} + \mathbf{p})\mathrm{d}\theta\mathrm{d}r\mathrm{d}z + \frac{1}{2}\iiint_V r\rho\dot{\mathbf{p}}^{\mathrm{T}}\dot{\mathbf{p}}\mathrm{d}\theta\mathrm{d}r\mathrm{d}z + \Omega\iiint_V r\rho\dot{\mathbf{p}}^{\mathrm{T}}\mathbf{J}(\mathbf{u} + \mathbf{p})\mathrm{d}\theta\mathrm{d}r\mathrm{d}z, \tag{9}$$

where V is the undeformed volume of the axisymmetric solid, ρ is the material density, and

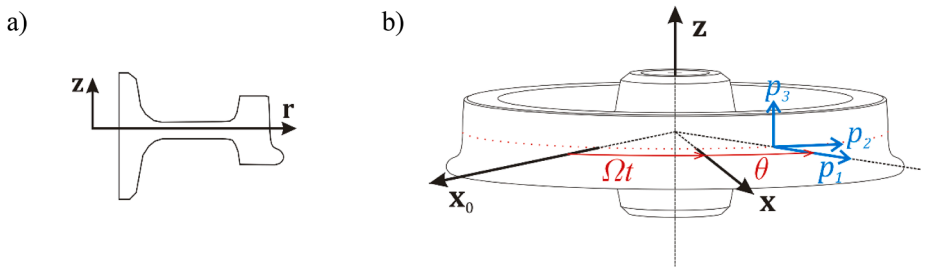

Fig. 1. Reference frame and coordinates: a) cross-section area of the wheel, b) visualisation of the geometry of revolution of the wheel.

$$\mathbf{E} = \mathbf{J}^{\mathrm{T}}\mathbf{J} = \begin{bmatrix} 1 & 0 & 0 \\ 0 & 1 & 0 \\ 0 & 0 & 0 \end{bmatrix}. \tag{10}$$

Substituting the previous Fourier series Eq. (3)

$$\begin{aligned} T = {} & \frac{1}{2}\Omega^2 \iiint_V r\rho \left(\mathbf{u} + \sum_{h=0}^{H} \left(\widetilde{\mathbf{p}}_h c_h + \overline{\mathbf{p}}_h s_h \right) \right)^{\mathrm{T}} \mathbf{E} \left(\mathbf{u} + \sum_{h=0}^{H} \left(\widetilde{\mathbf{p}}_h c_h + \overline{\mathbf{p}}_h s_h \right) \right) \mathrm{d}\theta \mathrm{d}r\mathrm{d}z \\ & + \frac{1}{2} \iiint_V r\rho \left(\sum_{h=0}^{H} \left(\dot{\widetilde{\mathbf{p}}}_h c_h + \dot{\overline{\mathbf{p}}}_h s_h \right) \right)^{\mathrm{T}} \left(\sum_{h=0}^{H} \left(\dot{\widetilde{\mathbf{p}}}_h c_h + \overline{\mathbf{p}}_h s_h \right) \right) \mathrm{d}\theta \mathrm{d}r\mathrm{d}z \\ & + \Omega \iiint_V r\rho \left(\sum_{h=0}^{H} \left(\dot{\widetilde{\mathbf{p}}}_h c_h + \overline{\mathbf{p}}_h s_h \right) \right)^{\mathrm{T}} \mathbf{J} \left(\mathbf{u} + \sum_{h=0}^{H} \left(\widetilde{\mathbf{p}}_h c_h + \overline{\mathbf{p}}_h s_h \right) \right) \mathrm{d}\theta \mathrm{d}r\mathrm{d}z, \end{aligned} \tag{11}$$

where $c_h = \cos\theta h$ and $s_h = \sin\theta h$ are defined for simplicity. At this point, FE methodology is adopted in order to derive the numerical model of the rotating solid. The cross-section of the wheelset is discretised in a 2D FE mesh. Let $\mathbf{p}^e$ be the displacements at the nodes of the e-th element of the FE mesh. The h-th harmonic displacements $\widetilde{\mathbf{p}}_h$ and $\overline{\mathbf{p}}_h$ in the e-th element domain can be approximated as follows:

$$\widetilde{\mathbf{p}}_h(r, \mathrm{z}) \approx \mathbf{N}^e(r, \mathrm{z}) \widetilde{\mathbf{p}}_h^e, \tag{12}$$

$$\overline{\mathbf{p}}_h(r, \mathrm{z}) \approx \mathbf{N}^e(r, \mathrm{z})\ \overline{\mathbf{p}}_h^e, \tag{13}$$

where $\mathbf{N}^e(r, \mathrm{z})$ contains the FE shape functions for the 2D cross-section mesh. Introducing this approach in Eq. (11) and performing the first integral with respect to the angular coordinate θ on the interval $[0, 2\pi]$, the kinetic energy for the e-th element can be rewritten as follows:

$$\begin{aligned} T^e = {} & \Omega^2 \left(\widetilde{\mathbf{p}}_0^{e\mathrm{T}} \mathbf{c}_0^e + \overline{\mathbf{p}}_0^{e\mathrm{T}} \mathbf{c}_0^e \right) + \frac{\Omega^2}{2} \widetilde{\mathbf{p}}_0^{e\mathrm{T}} \mathbf{b}^e \widetilde{\mathbf{p}}_0^e + \dot{\widetilde{\mathbf{p}}}_0^{e\mathrm{T}} \mathbf{m}^e \dot{\widetilde{\mathbf{p}}}_0^e + 2\Omega \dot{\overline{\mathbf{p}}}_0^{e\mathrm{T}} \mathbf{g}^e \widetilde{\mathbf{p}}_0^e + \frac{1}{2} \sum_{h=1}^{H} \Bigg[\Omega^2 \left(\widetilde{\mathbf{p}}_h^{e\mathrm{T}} \mathbf{b}^e \widetilde{\mathbf{p}}_h^e + \overline{\mathbf{p}}_h^{e\mathrm{T}} \mathbf{b}^e \overline{\mathbf{p}}_h^e \right) + \left(\dot{\widetilde{\mathbf{p}}}_h^{e\mathrm{T}} \mathbf{m}^e \dot{\widetilde{\mathbf{p}}}_h^e + \dot{\overline{\mathbf{p}}}_h^{e\mathrm{T}} \mathbf{m}^e \dot{\overline{\mathbf{p}}}_h^e \right) \\ & + \Omega \left(\dot{\widetilde{\mathbf{p}}}_h^{e\mathrm{T}} \mathbf{g}^e \widetilde{\mathbf{p}}_h^e + \dot{\overline{\mathbf{p}}}_h^{e\mathrm{T}} \mathbf{g}^e \overline{\mathbf{p}}_h^e \right) \Bigg] + \pi\Omega^2 \iint_{A^e} r\rho \mathbf{u}^{\mathrm{T}} \mathbf{E} \mathbf{u} \mathrm{d}r\mathrm{d}z \end{aligned} \tag{14}$$

where the integrals over the surface of each finite element area A^e result in the following matrices and vector:

$$\mathbf{m}^e = \pi \iint_{A^e} r\rho \mathbf{N}^{e\mathrm{T}} \mathbf{N}^e \mathrm{d}r\mathrm{d}z, \tag{15}$$

$$\mathbf{g}^e = 2\pi \iint_{A^e} r\rho \mathbf{N}^{e\mathrm{T}} \mathbf{J} \mathbf{N}^e \mathrm{d}r\mathrm{d}z, \tag{16}$$

$$\mathbf{b}^e = \pi \iint_{A^e} r\rho \mathbf{N}^{e\mathrm{T}} \mathbf{E} \mathbf{N}^e\, \mathrm{d}r\mathrm{d}z, \tag{17}$$

$$\mathbf{c}_0^e = 2\pi \iint_{A^e} r\rho \mathbf{N}^{e\mathrm{T}} \mathbf{E} \mathbf{u}\, \mathrm{d}r\mathrm{d}z = 2\pi \iint_{A^e} r^2 \rho \mathbf{N}^{e\mathrm{T}} \{\, 1 \quad 0 \quad 0 \,\}^{\mathrm{T}}\, \mathrm{d}r\mathrm{d}z. \tag{18}$$

These matrices are computed numerically through Gauss quadrature as in the standard FE method. Following the Lagrange equation procedure, the terms from the equation of motion that are obtained from the kinetic energy (14) are, for the harmonic $h = 0$,

$$\frac{\mathrm{d}}{\mathrm{d}t} \left(\frac{\partial T}{\partial \dot{\widetilde{\mathbf{p}}}_0^e} \right)^{\mathrm{T}} - \left(\frac{\partial T}{\partial \widetilde{\mathbf{p}}_0^e} \right)^{\mathrm{T}} = 2\mathbf{m}^e \ddot{\widetilde{\mathbf{p}}}_0^e + 2\Omega \mathbf{g}^e \dot{\overline{\mathbf{p}}}_0^e - 2\Omega^2 \mathbf{b}^e \widetilde{\mathbf{p}}_0^e - \Omega^2 \mathbf{c}_0^e, \tag{19}$$

and, for the remaining harmonics

$$\frac{\mathrm{d}}{\mathrm{d}t} \left(\frac{\partial T}{\partial \dot{\widetilde{\mathbf{p}}}_h^e} \right)^{\mathrm{T}} - \left(\frac{\partial T}{\partial \widetilde{\mathbf{p}}_h^e} \right)^{\mathrm{T}} = \mathbf{m}^e \ddot{\widetilde{\mathbf{p}}}_h^e + \Omega \mathbf{g}^e \dot{\overline{\mathbf{p}}}_h^e - \Omega^2 \mathbf{b}^e \widetilde{\mathbf{p}}_h^e. \tag{20}$$

The corresponding expression for the anti-symmetric terms $\overline{\mathbf{p}}_h^e$ is analogous. External forces are applied at wheelset points that do not rotate with the solid. Let $\mathbf{f}^e$ be an external force that is applied at a fixed point of the e th-element domain. The virtual work is calculated as follows

$$\delta W = \delta \mathbf{p}^e(r_F, z_F, -\Omega t)^{\mathrm{T}}\ \mathbf{f}^e, \tag{21}$$

with $(r_F, z_F, -\Omega t)$ being the cylindrical coordinates of the point at which the force is applied. Substituting Eqs. (3), (12) and (13) in Eq. (21), the virtual work becomes

$$\delta W = \left(\sum_{h=0}^{H} \delta \widetilde{\mathbf{p}}_h^{e\mathrm{T}}\ \mathbf{N}^e(r_F, z_F)^{\mathrm{T}} \cos\Omega h t - \sum_{h=1}^{H} \delta \overline{\mathbf{p}}_h^{e\mathrm{T}}\ \mathbf{N}^e(r_F, z_F)^{\mathrm{T}} \sin\Omega h t \right) \mathbf{f}^e. \tag{22}$$

From this last equation, the generalised forces associated with the coordinates $\widetilde{\mathbf{p}}_h^e$ and $\overline{\mathbf{p}}_h^e$ are, respectively

$$\widetilde{\mathbf{Q}}_h^e = \mathbf{N}^e(r_F, z_F)^{\mathrm{T}} \mathbf{f}^e \cos\Omega h t, \tag{23}$$

$$\overline{\mathbf{Q}}_h^e = -\mathbf{N}^e(r_F, z_F)^{\mathrm{T}} \mathbf{f}^e \sin\Omega h t. \tag{24}$$

Let $\widetilde{\mathbf{P}}_h$ and $\overline{\mathbf{P}}_h$ be the global coordinate vectors that contain the nodal coordinates of the FE mesh. The element matrices $\mathbf{m}^e$, $\mathbf{g}^e$, $\mathbf{b}^e$ and $\mathbf{c}_0^e$ in Eqs. (14)-(17) are assembled into global matrices following the standard FE procedure, giving the mass matrix $\mathbf{M}$, skew-symmetric gyroscopic matrix $\mathbf{G}$, stiffening matrix $\mathbf{B}$ and centrifugal force vector $\mathbf{c}_0$. The generalised force term $\mathbf{N}^e(r_F, z_F)^{\mathrm{T}}\mathbf{f}^e$ in Eqs. (23) and (24) can be also assembled in a global force vector $\mathbf{F}$. The resulting equation of motion for the rotating solid can be written as

$$2\mathbf{M}\ddot{\widetilde{\mathbf{P}}}_0 + 2\Omega\mathbf{G}\dot{\widetilde{\mathbf{P}}}_0 + \left(\mathbf{K}_0 - 2\Omega^2\mathbf{B}\right)\widetilde{\mathbf{P}}_0 = \mathbf{F} + \Omega^2\mathbf{c}_0, \tag{25}$$

$$\begin{bmatrix} \mathbf{M} & 0 \\ 0 & \mathbf{M} \end{bmatrix} \begin{Bmatrix} \ddot{\widetilde{\mathbf{P}}}_h \\ \ddot{\overline{\mathbf{P}}}_h \end{Bmatrix} + \Omega \begin{bmatrix} \mathbf{G} & 0 \\ 0 & \mathbf{G} \end{bmatrix} \begin{Bmatrix} \dot{\widetilde{\mathbf{P}}}_h \\ \dot{\overline{\mathbf{P}}}_h \end{Bmatrix} + \left(\mathbf{K}_h - \Omega^2 \begin{bmatrix} \mathbf{B} & 0 \\ 0 & \mathbf{B} \end{bmatrix} \right) \begin{Bmatrix} \widetilde{\mathbf{P}}_h \\ \overline{\mathbf{P}}_h \end{Bmatrix} = \begin{Bmatrix} \mathbf{F}\cos\Omega h t \\ -\mathbf{F}\sin\Omega h t \end{Bmatrix}, \quad h > 0, \tag{26}$$

where $\mathbf{K}_h$ is the standard stiffness matrix in the axisymmetric FE method [24]. The resulting equation of motion is linear since the angular velocity of the solid is assumed to be constant and the constitutive relationship is linear. As will be studied in the following section, the equation of motion also allows the eigenvalue problem to be solved, which provides the equivalent natural frequencies and mode shapes of the rotating solid.

The influence of the rotation on the results can be explained mathematically by the terms in the equation of motion that contain Ω. The gyroscopic term (involving $\mathbf{G}$) contains the product of the generalised-velocity vector and Ω, i.e. the Coriolis acceleration that couples radial and circumferential vibration of the flexible wheelset. In addition, there is one term that contains the product of Ω^2 and the generalised-displacement vector, the centripetal acceleration, thus producing the total stiffening matrix due to rotation, which in fact reduces the wheelset stiffness, sometimes referred to as spin softening [25].

3.2. Eulerian approach

From Eqs. (7) and (8), the displacements in the global Lagrangian coordinates and their derivatives can be easily calculated from those in the global Eulerian coordinates as follows

$$\widetilde{\mathbf{P}}_h = \widehat{c}_h \widetilde{\mathbf{W}}_h + \widehat{s}_h \overline{\mathbf{W}}_h, \tag{27}$$

$$\overline{\mathbf{P}}_h = -\widehat{s}_h \widetilde{\mathbf{W}}_h + \widehat{c}_h \overline{\mathbf{W}}_h, \tag{28}$$

$$\dot{\widetilde{\mathbf{P}}}_h = \widehat{c}_h \dot{\widetilde{\mathbf{W}}}_h + \widehat{s}_h \dot{\overline{\mathbf{W}}}_h - h\Omega\widehat{s}_h \widetilde{\mathbf{W}}_h + h\Omega\widehat{c}_h \overline{\mathbf{W}}_h, \tag{29}$$

$$\dot{\overline{\mathbf{P}}}_h = -\widehat{s}_h \dot{\widetilde{\mathbf{W}}}_h + \widehat{c}_h \dot{\overline{\mathbf{W}}}_h - h\Omega\widehat{c}_h \widetilde{\mathbf{W}}_h - h\Omega\widehat{s}_h \overline{\mathbf{W}}_h, \tag{30}$$

$$\ddot{\widetilde{\mathbf{P}}}_h = \widehat{c}_h \ddot{\widetilde{\mathbf{W}}}_h + \widehat{s}_h \ddot{\overline{\mathbf{W}}}_h - 2h\Omega\widehat{s}_h \dot{\widetilde{\mathbf{W}}}_h + 2h\Omega\widehat{c}_h \dot{\overline{\mathbf{W}}}_h - h^2\Omega^2\widehat{c}_h \widetilde{\mathbf{W}}_h - h^2\Omega^2\widehat{s}_h \overline{\mathbf{W}}_h, \tag{31}$$

$$\ddot{\overline{\mathbf{P}}}_h = -\widehat{s}_h \ddot{\widetilde{\mathbf{W}}}_h + \widehat{c}_h \ddot{\overline{\mathbf{W}}}_h - 2h\Omega\widehat{c}_h \dot{\widetilde{\mathbf{W}}}_h - 2h\Omega s_h \dot{\overline{\mathbf{W}}}_h + h^2\Omega^2\widehat{s}_h \widetilde{\mathbf{W}}_h - h^2\Omega^2\widehat{c}_h \overline{\mathbf{W}}_h, \tag{32}$$

where $\widehat{c}_h = \cos\Omega h t$ and $\widehat{s}_h = \sin\Omega h t$. Eqs. (27) to (32) are substituted into Eq. (26) (in the first block), which yields

$$\begin{aligned} &\cos\Omega h t \left(\mathbf{M}\ddot{\widetilde{\mathbf{W}}}_h + 2h\Omega\mathbf{M}\dot{\overline{\mathbf{W}}}_h - h^2\Omega^2\mathbf{M}\widetilde{\mathbf{W}}_h + \Omega\mathbf{G}\dot{\widetilde{\mathbf{W}}}_h + h\Omega^2\mathbf{G}\overline{\mathbf{W}}_h - \Omega^2\mathbf{B}\widetilde{\mathbf{W}}_h - \mathbf{F} + \mathbf{F}_1^E \right) \\ &+\sin\Omega h t \left(\mathbf{M}\ddot{\overline{\mathbf{W}}}_h - 2h\Omega\mathbf{M}\dot{\widetilde{\mathbf{W}}}_h - h^2\Omega^2\mathbf{M}\overline{\mathbf{W}}_h + \Omega\mathbf{G}\dot{\overline{\mathbf{W}}}_h - h\Omega^2\mathbf{G}\widetilde{\mathbf{W}}_h - \Omega^2\mathbf{B}\overline{\mathbf{W}}_h + \mathbf{F}_2^E \right) = 0, \end{aligned} \tag{33}$$

where $\mathbf{F}_1^E$ and $\mathbf{F}_2^E$ contain the elastic forces (the terms of the equation of motion that are multiplied by $\mathbf{K}_h$). Bearing in mind that the equation must be fulfilled for any instant, each of the expressions between brackets multiplied by $\cos\Omega h t$ or by $\sin\Omega h t$ must be equal to

zero independently. Consequently, Eq. (33) can be separated in two, and combined in matrix blocks, giving

$$\begin{bmatrix} \mathbf{M} & 0 \\ 0 & \mathbf{M} \end{bmatrix} \begin{Bmatrix} \ddot{\widetilde{\mathbf{W}}}_h \\ \ddot{\overline{\mathbf{W}}}_h \end{Bmatrix} + \Omega \begin{bmatrix} \mathbf{G} & 2h\mathbf{M} \\ -2h\mathbf{M} & \mathbf{G} \end{bmatrix} \begin{Bmatrix} \dot{\widetilde{\mathbf{W}}}_h \\ \dot{\overline{\mathbf{W}}}_h \end{Bmatrix} + \left(\mathbf{K}_h - \Omega^2 \begin{bmatrix} \mathbf{B} + h^2\mathbf{M} & -h\mathbf{G} \\ h\mathbf{G} & \mathbf{B} + h^2\mathbf{M} \end{bmatrix} \right) \begin{Bmatrix} \widetilde{\mathbf{W}}_h \\ \overline{\mathbf{W}}_h \end{Bmatrix} = \begin{Bmatrix} \mathbf{F} \\ \mathbf{0} \end{Bmatrix}. \tag{34}$$

It must be highlighted that the matrix $\mathbf{K}_h$ is independent of the approach (Lagrangian or Eulerian). The equation for harmonic 0 is

$$2\mathbf{M}\ddot{\widetilde{\mathbf{W}}}_0 + 2\Omega\mathbf{G}\dot{\widetilde{\mathbf{W}}}_0 + \left(\mathbf{K}_0 - 2\Omega^2\mathbf{B}\right)\widetilde{\mathbf{W}}_0 = \mathbf{F} + \Omega^2\mathbf{c}_0. \tag{35}$$

4. Results

The results shown in the present section are intended to provide understanding of the effects of rotation on the dynamics of the railway wheelset through the analysis of the rotating natural frequencies and the strains at wheel web positions. This analysis will also allow simulation of the measurements made by instrumented wheelsets at high frequency and speed. The wheelset and FE mesh shown in Fig. 2 are adopted, with nominal wheel diameter of 860 mm. In this model, the nodes that correspond to location of the axle boxes have been clamped as a boundary condition. While this boundary condition may result in a reduced accuracy of the model, particularly in the frequency bands where the wheelset axle modes are present, it is a common kinematic constraint used in instrumented wheelset studies (e.g., Ref. [26]). This is because it enables the use of a positive-definite stiffness matrix, which is essential for performing static calculations. Given that this study aims to compare both static and dynamic calculations, it was deemed preferable to apply the same conditions to all calculations for consistency. Alternative, constraints can also be considered within the current modelling approach, such as the free wheelset or the addition of elastic supports at the axle boxes. However, the combination of very high stiffnesses in the wheelset with very low support stiffnesses of the primary suspension can lead to numerical errors.

4.1. Natural frequencies and equivalent natural frequencies

Table 1 presents information associated with the natural frequencies of the wheelset. These frequencies are obtained by solving an eigenvalue problem from the Lagrangian formulation (26) and the Eulerian formulation (34), obtaining the frequencies indicated in the table as ω_L and ω_E respectively (all the results in the table are expressed in Hz). In order to make the rotation effects more noticeable, the speed of the wheelset has been chosen to be sufficiently high (300 km/h, which corresponds to $\Omega = 195.39$ rad/s $=$ 31.10 Hz). The modes have also been calculated for the non-rotating case by setting $\Omega = 0$ (these frequencies are identified as ω_0, and they are listed in the third column of the table). The wheelset mode shapes of the first eight modes obtained for the non-rotating case are shown in Fig. 3.

The second column of Table 1 shows the number of nodal diameters of the non-rotating wheelset. The fifth and sixth columns contain the corresponding frequencies of the rotating wheelset obtained through the Lagrangian and Eulerian models, respectively. The non-rotating modes with $h > 0$ split into two frequencies when the angular velocity is non-zero; the difference between the split frequencies is more noticeable for the Eulerian model. In column 4 the whirl direction of the rotating modes is identified as forward (fw) and backward (bw) waves.

The pair of frequencies that are split in the Eulerian model are known as forward and backward frequencies, and their respective value can be estimated through the formulae $\omega_0 + h\Omega$ and $\omega_0 - h\Omega$ (see seventh column), which were developed for wheels with a rotating force in [13], ω_0 being the non-rotating natural frequency. The error of the estimate $\omega_0 \pm h\Omega$ with respect to the exact frequency for the rotating system (Eulerian frequency ω_E) is listed in column 8. The formulae $\omega_0 \pm h\Omega$ as an estimation of the Euler frequencies can also be deduced through Eq. (26) when rotating effects are neglected by setting $\Omega = 0$ (except in the force term), deducing the following equation:

$$\begin{bmatrix} \mathbf{M} & 0 \\ 0 & \mathbf{M} \end{bmatrix} \begin{Bmatrix} \ddot{\widetilde{\mathbf{P}}}_h \\ \ddot{\overline{\mathbf{P}}}_h \end{Bmatrix} + \mathbf{K}_h \begin{Bmatrix} \widetilde{\mathbf{P}}_h \\ \overline{\mathbf{P}}_h \end{Bmatrix} = \begin{Bmatrix} \mathbf{F}\cos\Omega ht \\ -\mathbf{F}\sin\Omega ht \end{Bmatrix}. \tag{36}$$

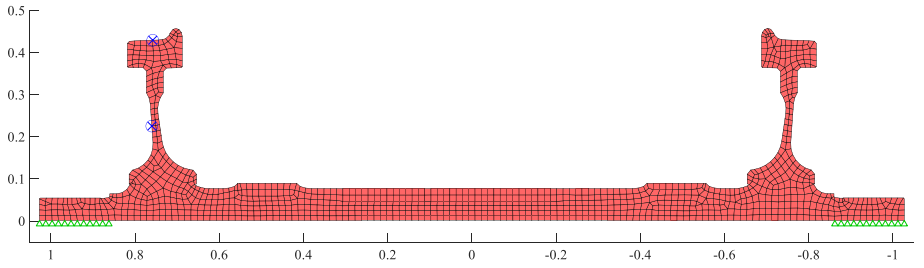

Fig. 2. Wheelset FE mesh (two wheels and axle). Mark ⊗ shows the nodes where the wheel-rail contact force is applied, and the strain is measured. Mark Δ shows the nodes that are constrained.

Table 1
Natural frequencies and equivalent natural frequencies of the rotating wheel.

			Natural frequencies [Hz]						
	Nodal diameters (h)	$\Omega = 0$	$\Omega = 195.39$rad/s $= 31.10$ Hz; $V = 300$km/h						
		ω_0	Whirl	Lagrange ω_L	Euler ω_E	$\omega_0 \pm h\Omega$	$\omega_0 \pm h\Omega$(error)	$\omega_L - h\Omega$	$\omega_L + h\Omega$
1	0	73.089	–	66.129	66.129	73.089	+10.52%	66.129	
2	1	104.456	fw	88.713	119.810	135.553	+13.14%		119.810
			bw	115.809	84.712	73.359	−13.40%	84.712	
3	1	152.493	fw	149.986	181.083	183.590	+1.38%		181.083
			bw	154.364	123.267	121.396	−1.52%	123.267	
4	1	230.074	fw	214.224	245.321	261.172	6.46%		245.321
			bw	249.599	218.501	198.977	−8.94%	218.501	
5	0	266.987	–	266.977	266.977	266.987	0.00%	266.977	
6	0	269.917	–	269.907	269.907	269.917	0.00%	269.907	
7	1	373.129	fw	344.594	375.691	404.226	7.60%		375.691
			bw	402.001	370.904	342.031	−7.78%	370.904	
8	2	411.364	fw	409.358	471.552	473.558	0.43%		471.552
			bw	413.227	351.033	349.170	−0.53%	351.033	
9	2	411.762	fw	409.751	471.946	473.956	0.43%		471.946
			bw	413.630	351.436	349.568	−0.53%	351.436	
10	1	560.531	fw	529.884	560.981	591.628	5.46%		560.981
			bw	591.151	560.054	529.433	−5.47%	560.054	
11	1	890.444	fw	860.848	891.945	921.541	3.32%		891.945
			bw	919.960	888.863	859.347	−3.32%	888.863	
12	3	1103.894	fw	1100.65	1193.94	1197.18	0.27%		1193.94
			bw	1107.04	1013.75	1010.60	−0.31%	1013.75	
13	3	1105.029	fw	1101.78	1195.07	1198.32	0.27%		1195.07
			bw	1108.18	1014.89	1011.74	−0.31%	1014.89	
14	0	1144.283	–	1144.27	1144.27	1144.28	0.00%	1144.27	
15	0	1242.254	–	1241.85	1241.86	1242.25	0.03%	1241.86	

Assuming that the excitation is sinusoidal with frequency ω, the previous equation becomes

$$\begin{bmatrix} \mathbf{M} & 0 \\ 0 & \mathbf{M} \end{bmatrix} \begin{Bmatrix} \ddot{\widetilde{\mathbf{P}}}_h \\ \ddot{\overline{\mathbf{P}}}_h \end{Bmatrix} + \mathbf{K}_h \begin{Bmatrix} \widetilde{\mathbf{P}}_h \\ \overline{\mathbf{P}}_h \end{Bmatrix} = \begin{Bmatrix} \mathbf{F}\ \cos\omega t\ \cos\Omega h t \\ -\mathbf{F}\ \cos\omega t\ \sin\Omega h t \end{Bmatrix}. \tag{37}$$

From basic trigonometry relationships, the force term can be rewritten as follows

$$\begin{bmatrix} \mathbf{M} & 0 \\ 0 & \mathbf{M} \end{bmatrix} \begin{Bmatrix} \ddot{\widetilde{\mathbf{P}}}_h \\ \ddot{\overline{\mathbf{P}}}_h \end{Bmatrix} + \mathbf{K}_h \begin{Bmatrix} \widetilde{\mathbf{P}}_h \\ \overline{\mathbf{P}}_h \end{Bmatrix} = \frac{1}{2} \begin{Bmatrix} \mathbf{F}(\cos((\omega + \Omega h)t) + \cos((\omega - \Omega h)t)) \\ \mathbf{F}(-\sin((\omega + \Omega h)t) + \sin((\omega - \Omega h)t)) \end{Bmatrix}. \tag{38}$$

From the previous expression, it can be deduced that the system enters into resonance when some non-rotating natural frequency coincides with $\omega + h\Omega$, or $\omega - h\Omega$, which justifies the estimation of the natural frequencies according to [13]. Consequently, the natural frequencies calculated through the formulae $\omega_0 + h\Omega$ and $\omega_0 - h\Omega$ will have a higher error relative to the frequencies provided by the Euler model in those cases in which the inertial effects associated with the rotation are significant.

The forward and backward frequencies from the Eulerian model correspond to those at which the rotating solid vibrates in its free response, as seen from a non-rotating observer. The corresponding free response consists of waves that rotate in either forward (co-rotating with the wheelset) or backward directions (counter-rotating). The natural frequencies of the Lagrangian model are associated with the wheelset free response viewed from a reference that rotates with the solid. Therefore, the Lagrangian model provides intrinsic information of the rotating solid. The difference between the non-rotating frequencies ω_0 and those calculated by the Lagrangian model ω_L indicates the influence of the inertial effects due to the wheel rotation. The Coriolis force, which acts perpendicular to the axis of rotation, causes changes in the speed of the two rotating waves relative to the moving frame for mode pairs with $h > 0$. Changes in the kinetic energy or inertia of the rotating solid due to the work done by the inertial Coriolis force cause the divergence of the natural frequencies associated with these waves. The centrifugal effects, from the term containing Ω^2, alter the frequencies of both modes equally, but these changes are usually small for conventional railway speeds, as also found in [18].

Consequently, the forward and backward modes calculated by the Eulerian model are actually composed of motions corresponding to the vibration of the solid and its rotation. Furthermore, the Eulerian frequencies ω_E can be calculated more precisely from the Lagrangian frequencies ω_L through the following equation:

$$\omega_E = \omega_L \pm h\Omega. \tag{39}$$

This result is reflected in columns 9 and 10 of Table 1. The error associated with Eq. (39) is negligible for all calculated modes (the maximum error obtained is 5.32×10^{-11}). The mathematical proof of Eq. (39) is presented below.

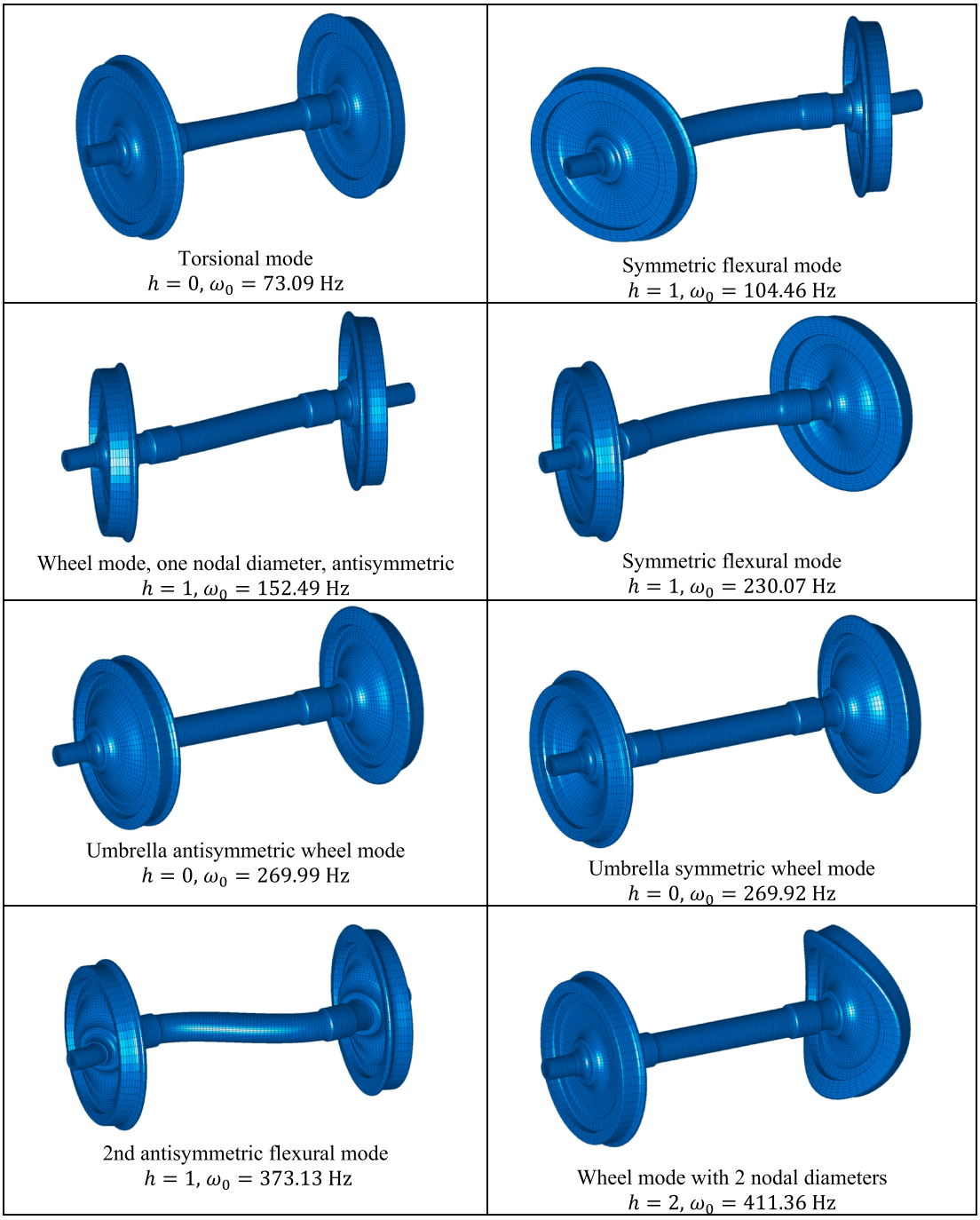

Fig. 3. Mode shapes of non-rotating wheelset corresponding to the first eight natural.

Let $\mathbf{P}_h^*$ be an eigenvector corresponding to the Lagrangian model and ω_L the corresponding natural frequency. From the coordinate transformation in Eqs. (27) and (28) and extending the previous equations to the complex domain, the eigenvector $\mathbf{P}_h^*$ expressed through Eulerian coordinates $\mathbf{W}_h$ is

$$\mathbf{P}_h^* e^{i\omega_L t} = \begin{bmatrix} e^{ih\Omega t} & -i\, e^{ih\Omega t} \\ i\, e^{ih\Omega t} & e^{ih\Omega t} \end{bmatrix} \mathbf{W}_h \tag{40}$$

or

$$\mathbf{P}_h^* e^{i\omega_L t} = \begin{bmatrix} 1 & -i \\ i & 1 \end{bmatrix} \mathbf{W}_h e^{i(\omega_L + h\Omega)t}, \tag{41}$$

from which it follows that the eigenvector in the Eulerian model is

$$\mathbf{W}_h^* = \begin{bmatrix} 1 & -i \\ i & 1 \end{bmatrix} \mathbf{W}_h, \tag{42}$$

and the natural frequency is exactly $\omega_L + h\Omega$. Hence, it is proved that the natural frequencies of the Eulerian model are calculated accurately from those of the Lagrangian model through Eq. (39).

The amount of the frequency split in the Lagrangian frame due to inertial effects depends on the shape of the wheelset mode and its rotational velocity. When comparing two modes that originate from the same non-rotating mode (with $h > 0$), one of the two Lagrangian mode shapes is associated with a lower and the other with a higher natural frequency. The trend of the Lagrangian modes listed in Table 1 is as follows: The forward waves have a lower natural frequency, meaning the frequency decreases with increasing rotational velocity, while for the backward waves the frequency increases. The absolute velocity of the wheelset particles is greater in a deformation that rotates in the same direction as Ω (the absolute velocity is the sum of the relative velocity and velocity due to Ω). As a result, these Lagrangian modes have more kinetic energy, meaning they have more equivalent mass, and their natural frequency is lowered. Conversely, the natural frequency is increasing for the Lagrangian modes where the deformation rotates in the opposite direction to Ω and has less equivalent mass associated. If the rotation speed of the wheelset remains subcritical ($\Omega < \omega_L$), a forward mode in moving axes obtained from the Lagrangian model remains a forward mode obtained with the Eulerian model in fixed axes (and vice versa). This is even true for high-speed railway vehicles. Nevertheless, the Eulerian forward mode has a higher frequency than the backward mode. This is because the wave speed seen from fixed axes is the sum of the wheelset rotation speed Ω and the speed of the Lagrangian forward wave ($c = \omega_L/h$), which is co-rotating with the wheelset. The backwards mode is observed at a reduced frequency as the direction of wheelset rotation is opposite to the Lagrangian backward wave. Modes with $h = 0$ are observed at the same frequency in both frames.

In Fig. 4 the Campbell diagram of the wheelset modes listed in Table 1 is presented for both models. It can be seen that the variations between forward and backward frequencies are generally smaller for the Lagrangian model (Fig. 4a). The modes that present greater divergence in this frame are more affected by the inertial effects due to rotation, as observed in Table 1 at 300 km/h (maximum speed of the diagram) for modes 4, 7, 10 and 11. All of them are 1-nodal-diameter modes and have a radial component due to the axle bending, which is coupled with the wheel vibration. The divergence of these modes in the Eulerian model (Fig. 4b) is smaller, while axial modes have a larger frequency split in this frame, especially the axial 2-nodal- and 3-nodal-diameter modes.

4.2. Strain gauge configurations for instrumented wheels

The response that would be measured by an instrumented wheelset is studied for different types of excitation, which correspond to the vertical force transmitted through the wheel-rail contact; cases with constant and sinusoidal forces are evaluated for different wheelset angular velocities. The calculated response will correspond to the combination of the strains at some specific points on the web wheel, as these are added (or subtracted) in the instrumented wheelset. This calculation is carried out through the post-processing of the results of the Lagrangian formulation. The applied vertical force and the measured strain are associated with the nodes marked in Fig. 2.

The location of these measurement points is determined by the instrumentation strategy presented in Ref. [26], which is adopted in this work for the analysis of instrumented wheelsets. The objective of the instrumentation is to obtain pairs of measurement channels

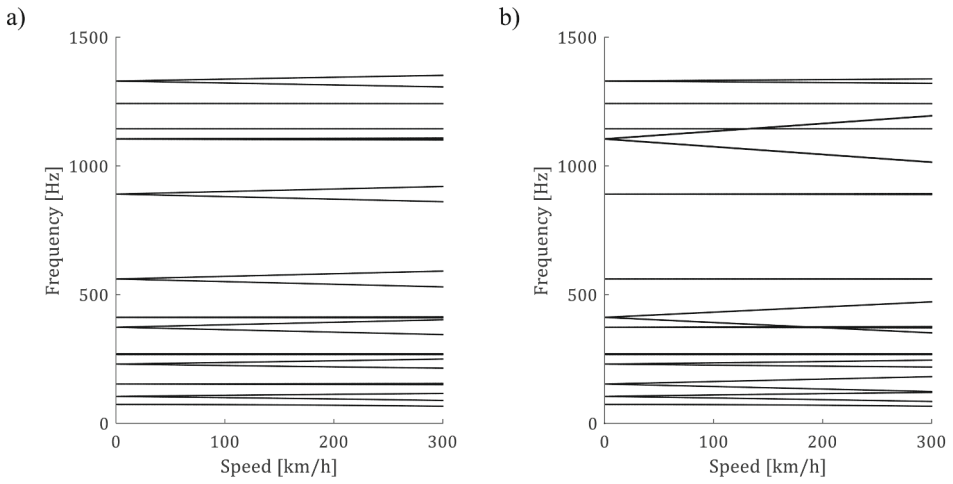

Fig. 4. Campbell diagram calculated for the Lagrangian (a) and Eulerian (b) model.

that provide, for a constant applied load, pure (tonal) harmonic signals as a function of the angle rotated by the wheelset. To this end, two strain gauge bridges like the ones shown in Fig. 6 are used, rotated one from the other by 90°. The signal amplitude of each channel will be proportional to the force applied to the wheel-rail contact, and the arrangement of the instrumentation in the wheel web will cause the sinusoidal signals from the two channels to be out of phase by 90°, that is

$$S_1 = QG\cos\theta, \tag{43}$$

$$S_2 = QG\cos\left(\theta + \frac{\pi}{2}\right), \tag{44}$$

S_c being the signal of channel nr. c, G the circuit gain, Q the wheel/rail contact force and θ the wheel angle. According to this strategy, the combined modulus of the two signals is proportional to the transmitted force, regardless of the angular position of the wheelset

$$Q = \frac{\sqrt{S_1^2 + S_2^2}}{G}. \tag{45}$$

According to Ref. [26], the strain gauges are mounted on the wheel web to measure the radial strain. Fig. 5 shows the static measurement ($\Omega = 0$) from a Wheatstone bridge with a single strain gauge, when a constant vertical load $Q = 100$ kN is applied in the wheel/rail contact. This result is obtained as a function of the wheel rotation angle. In this figure, it can be seen that the measurement provided by a single strain gauge on the wheel web is far from being purely harmonic. However, this signal as a function of the angle of rotation of the wheelset can be considered 2π-periodic and can be expanded as a Fourier series. By combining two strain gauges fixed on the same diametral line on opposite radii (at 0° and 180°, see Fig. 6a), the resulting signal removes the even harmonics of the Fourier series, including the 0-harmonic. In this way, it also suppresses the centrifugal forces (the term $\Omega^2\mathbf{c}_0$ of Eq. (25)) and temperature effects (thermal drift) are compensated. When the previous assembly is duplicated by rotating it by 60° (180°/3) as shown in Fig. 6b, the 3rd harmonic is also eliminated. If the assembly in Fig. 6b is duplicated again by rotating it by 36° (180°/5), the 5th harmonic is also removed, obtaining the layout represented in Fig. 6c. Finally, the configuration adopted in this work uses 16 strain gauges, the position of which is obtained by duplicating the assembly of Fig. 6c and rotating it by 25.71° (180°/7) to suppress the 7th harmonic. The different signals for a constant force at very low speed are shown in Fig. 5 for the different layouts. It is observed how the configuration with 16 strain gauges allows a practically pure sinusoidal signal to be measured, so that it is possible to establish the value of the transmitted force accurately from the amplitude of the measured strain.

4.3. Response to a vertical constant force

Next, the response is computed to a constant vertical force Q applied to the wheel-rail contact point at different speeds. The displacements are calculated through the Lagrangian formulation using Eq. (25) for the harmonic $h = 0$ and Eq. (26) for the remaining harmonics as follows

$$\widetilde{\mathbf{P}}_0 = \mathbf{D}_0(0)^{-1}\left(\mathbf{F} + \Omega^2\mathbf{c}_0\right), \tag{46}$$

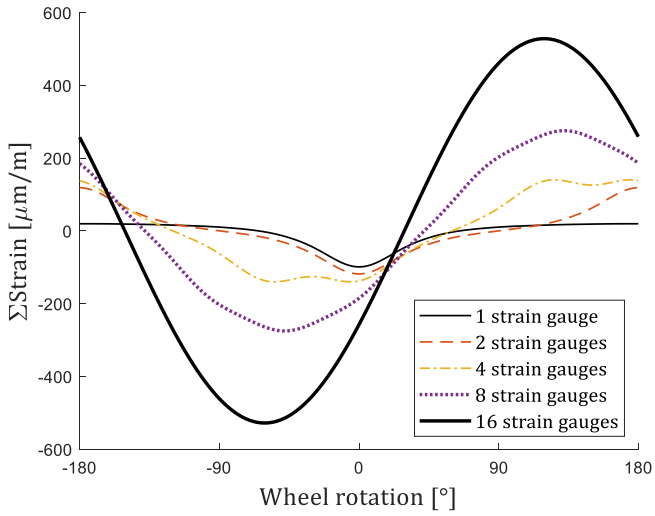

Fig. 5. Simulation of the signal at very low speed for the strain measured along one wheel rotation by five instrumentation layouts: 1, 2, 4, 8 and 16 strain gauges. The applied force is 100 kN (constant) and the angular velocity Ω is 0.

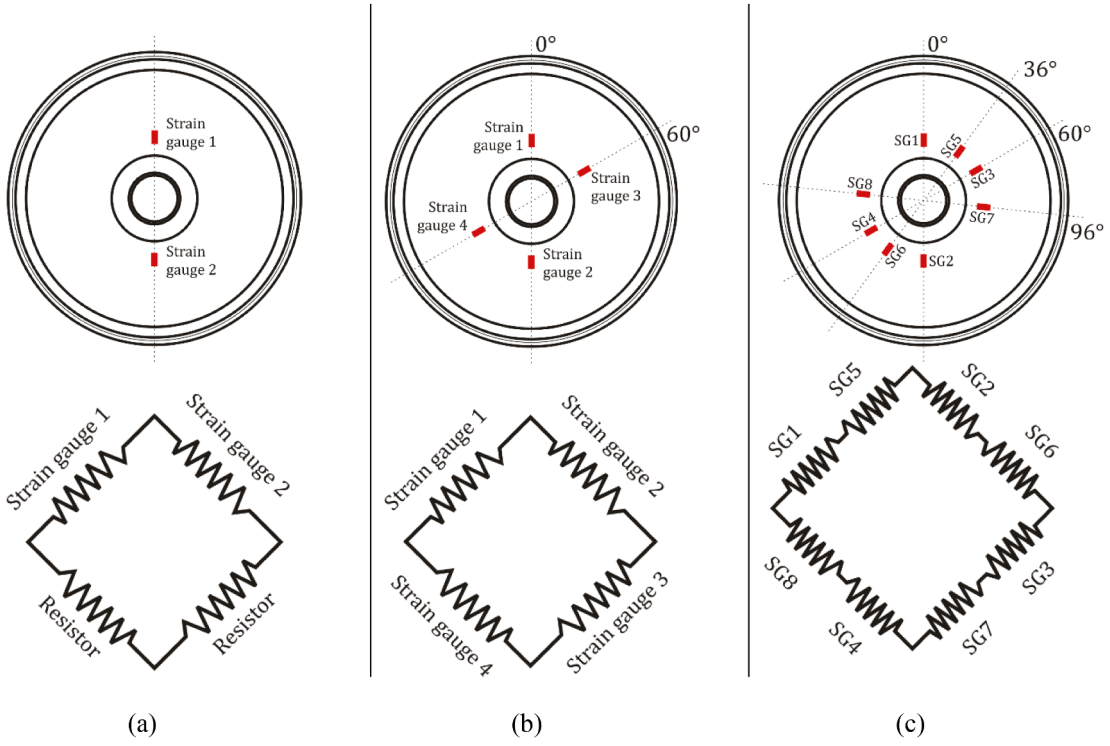

Fig. 6. Three strain gauge configurations. Layout in the wheel web (upper) and the corresponding Wheatstone bridge (lower): a) two strain gauges, b) four strain gauges, c) eight strain gauges.

$$\begin{Bmatrix} \widetilde{\mathbf{P}}_h \\ \overline{\mathbf{P}}_h \end{Bmatrix} = \mathbf{D}_h(h\Omega)^{-1} \begin{Bmatrix} \mathbf{F} \\ \mathrm{i}\mathbf{F} \end{Bmatrix} \mathrm{e}^{\mathrm{i}h\Omega t}, \tag{47}$$

where

$$\mathbf{D}_0(\omega) = \mathbf{K}_0 - 2\Omega^2\mathbf{B} + 2\mathrm{i}\omega\Omega\mathbf{G} - 2\omega^2\mathbf{M}, \tag{48}$$

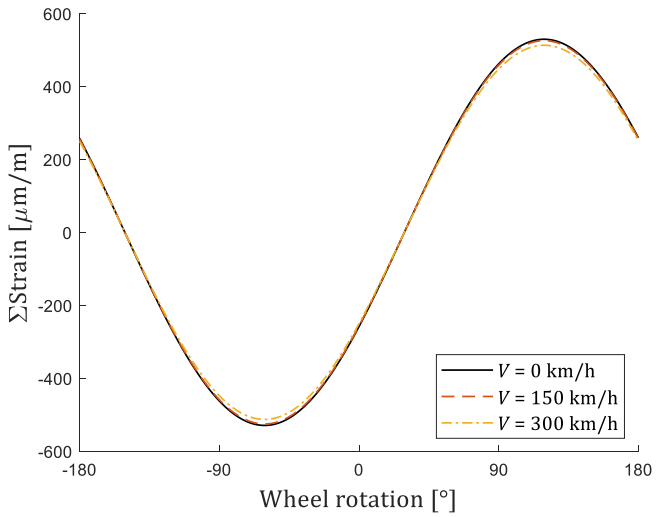

Fig. 7. Simulation of the signal for the strain measured along one-wheel rotation for three different speeds through the 16-gauge configuration. The applied force is 100 kN (constant).

$$\mathbf{D}_h(\omega) = \mathbf{K}_h - \Omega^2 \begin{bmatrix} \mathbf{B} & 0 \\ 0 & \mathbf{B} \end{bmatrix} + \mathrm{i}\omega\Omega \begin{bmatrix} \mathbf{G} & 0 \\ 0 & \mathbf{G} \end{bmatrix} - \omega^2 \begin{bmatrix} \mathbf{M} & 0 \\ 0 & \mathbf{M} \end{bmatrix} \tag{49}$$

In Fig. 7, the combination of strains corresponding to the 16-gauge Wheatstone bridge is shown, calculated at very low speed, at 150 and at 300 km/h. The results suggest a very small influence of the speed for constant forces, once the centrifugal effect has been suppressed. This is indicative of the robustness of the force measurement method regardless of the wheelset angular velocity.

4.4. Response to a vertical sinusoidal force

Extending the study from the previous section, a force is considered with a sinusoidal component at frequency ω (added to the constant value) that is applied to the rotating wheelset. As seen in Eqs. (26) and (38), the equation of motion for the h-th harmonic associated with a sinusoidal excitation is

$$\begin{bmatrix} \mathbf{M} & 0 \\ 0 & \mathbf{M} \end{bmatrix} \begin{Bmatrix} \ddot{\widetilde{\mathbf{P}}}_h \\ \ddot{\overline{\mathbf{P}}}_h \end{Bmatrix} + \Omega \begin{bmatrix} \mathbf{G} & 0 \\ 0 & \mathbf{G} \end{bmatrix} \begin{Bmatrix} \dot{\widetilde{\mathbf{P}}}_h \\ \dot{\overline{\mathbf{P}}}_h \end{Bmatrix} + \left(\mathbf{K}_h - \Omega^2 \begin{bmatrix} \mathbf{B} & 0 \\ 0 & \mathbf{B} \end{bmatrix} \right) \begin{Bmatrix} \widetilde{\mathbf{P}}_h \\ \overline{\mathbf{P}}_h \end{Bmatrix} = \frac{1}{2} \begin{Bmatrix} \mathbf{F}\ (\cos((\omega + h\Omega)t) + \cos((\omega - h\Omega)t)) \\ \mathbf{F}\ (-\sin((\omega + h\Omega)t) + \sin((\omega - h\Omega)t)) \end{Bmatrix} \tag{50}$$

This result implies that, when a sinusoidal non-rotating force acts on a rotating solid, the solid is excited at frequencies $\omega + h\Omega$ and $\omega - h\Omega$. From this, the response due to a sinusoidal force is obtained as

$$\begin{Bmatrix} \widetilde{\mathbf{P}}_h \\ \overline{\mathbf{P}}_h \end{Bmatrix} = \frac{1}{2}\mathbf{D}_h(\omega + h\Omega)^{-1} \begin{Bmatrix} \mathbf{F} \\ \mathrm{i}\mathbf{F} \end{Bmatrix} \mathrm{e}^{\mathrm{i}(\omega + h\Omega)t} + \frac{1}{2}\mathbf{D}_h(\omega - h\Omega)^{-1} \begin{Bmatrix} \mathbf{F} \\ -\mathrm{i}\mathbf{F} \end{Bmatrix} \mathrm{e}^{\mathrm{i}(\omega - h\Omega)t}, \tag{51}$$

where $\mathbf{D}_h$ is defined in Eq. (46).

In order to evaluate the effect of the application of a sinusoidal force on the wheelset, a force defined as $Q_a(t) = Q_0 + Q_1 \cos\omega t$ is applied, with a mean value of $Q_0 = 100$ kN, a variable amplitude of $Q_1 = 25$ kN and an excitation frequency ω of 20 Hz, which is the highest frequency at which instrumented wheelsets are usually required to measure [20]. Fig. 8 compares the actual applied force, $Q_a(t)$, and the one measured through the instrumentation used, $Q_m(t)$. The abscissa axis gives the rotation of the wheelset directly in revolutions. At 150 km/h (Fig. 8a), the simulation provides a measured force very similar to actual one. Fig. 8b shows that the error considerably increases at 300 km/h, although it remains at a deviation of 4.03 kN (3.2%) for the maximum peak. It is concluded that at high speeds, the measurement procedure underestimates the value of the force, thus not being on the side of safety.

Changing the excitation frequency, results are shown in Fig. 9 for 100 Hz and 1000 Hz at a speed of 150 km/h. Applying an excitation frequency of 100 Hz, Fig. 9a shows that the measured force is now overestimated as a result of a dynamic amplification phenomenon. The opposite effect (mechanical filtering) is observed in Fig. 9b when the force is applied with a frequency of 1000 Hz, providing a strong underestimation of the measured force. Moreover, the phase of the measured force is reversed compared with the actual one.

Table 2 shows the maximum, minimum and mean values and the amplitudes of the forces measured for the cases presented in Figs. 8 and 9. In the calculations presented for Fig. 8, which correspond to a type of measurement associated with UIC leaflet 518, the measured force is underestimated and the error increases as the rotation speed increases. Moreover, the error is also found to increase as the force variation frequency increases. This is due to the dynamic impedance associated with the wheelset's inertia, which reduces the wheelset response and consequently, the strains. In the measurements presented in Fig. 9, the analysed frequencies are in the band where resonances and anti-resonances of the wheelset appear, which can produce amplification or filtering in the wheelset's response

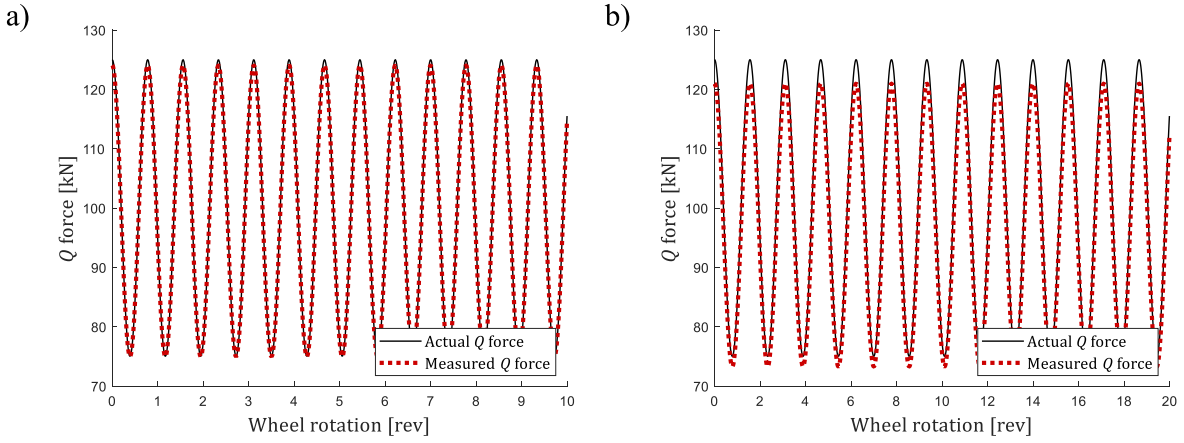

Fig. 8. Comparison between the applied force at 20 Hz (input) and the simulated force measured for the 16-gauge configuration for a vehicle speed of: a) 150 km/h, b) 300 km/h.

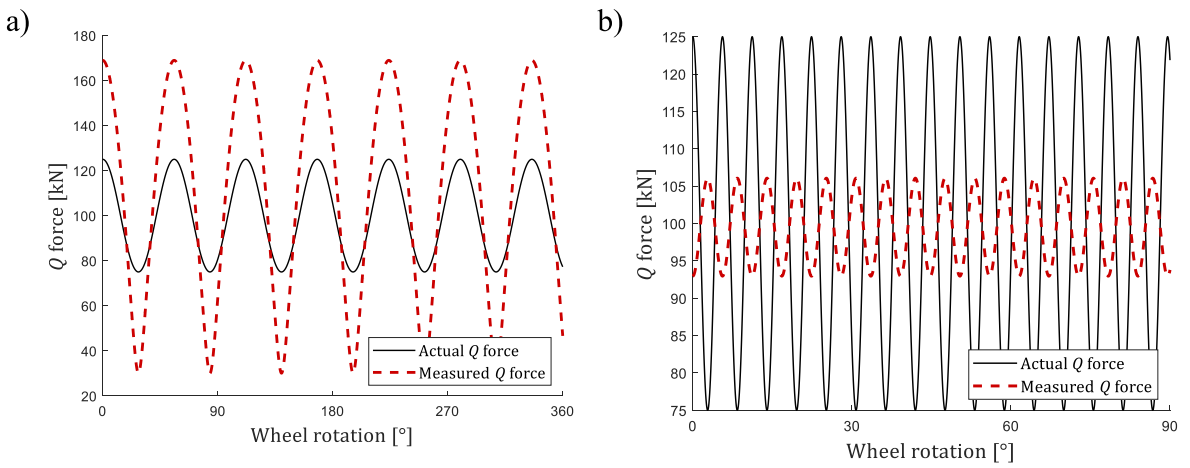

Fig. 9. Comparison between the actual force and the simulated force measured for the 16-gauge configuration for a vehicle speed of 150 km/h with an excitation frequency of: a) 100 Hz, b) 1000 Hz.

Table 2
Maximum, minimum, mean and amplitude of the forces plotted in Figs. 8 and 9. The table includes the error in the measurement of both the mean and the amplitude of force, which is indicated in parentheses as a percentage.

	Actual force	Measured force			
	All figures	150 km/h 20 Hz	300 km/h 20 Hz	150 km/h 100 Hz	150 km/h 1000 Hz
		Fig. 8a	Fig. 8b	Fig. 9a	Fig. 9b
Maximum	125 kN	124.07 kN	120.98 kN	168.93 kN	106.06 kN
Minimum	75 kN	74.09 kN	73.27 kN	30.07 kN	92.94 kN
Mean	100 kN	99.50 kN (0.49%)	97.13 kN (2.87%)	99.50 kN (0.49%)	99.50 kN (0.49%)
Amplitude	25 kN	24.56 kN (1.75%)	23.85 kN (4.58%)	69.43 kN (177.72%)	6.56 kN (73.76%)

that respectively produce overestimation or underestimation of the applied force through the measurement.

In order to show the relation between the levels (amplitudes) of the measured force Q_m and the actual one Q_a, a sweep over the excitation frequency is made for three speeds: 0, 150 and 300 km/h. In these calculations, the actual force is sinusoidal with frequency ω. Fig. 10 shows the diagram for the ratio Q_m/Q_a, giving a constant value of 1 at low frequencies, which indicates that the instrumented wheelset measures satisfactorily the level of force applied. According to this result, the procedure guarantees the precision of the measurements up to the maximum frequency required for instrumented wheelsets, independent of the wheelset rotation speed. As the speed increases, however, measurement inaccuracies occur earlier and appear from 20 Hz at 300 km/h (at 300 km/h and 30 Hz, the error is 3.7%; at very low speed and 60 Hz, the error is 5.53%). As seen in Fig. 9a and Fig. 9b, it is observed that the level of force measured at 150 km/h is slightly above the actual one for 100 Hz (force amplification), while the ratio Q_m/Q_a is significantly smaller than 1 for 1000 Hz (force filtration); at other frequencies the differences can be larger.

The splitting of the non-rotating peaks from the 0 km/h curve when rotation is introduced is consistent with the Campbell diagram (Fig. 4b) for the Eulerian model at 150 and 300 km/h. As a consequence of the rotation, a sinusoidal force applied at frequency ω can produce resonance if $\omega \pm h\Omega$ coincide with a natural frequency of the rotating solid calculated for the h-th harmonic through the Lagrangian model. This effect can be seen in Fig. 10 through the resonance splitting in the rotating cases.

It is remarkable that Fig. 10 contains fewer resonances than might be expected from the Campbell diagram (Fig. 4b) and the frequencies listed in Table 1. This is the case for the mode with non-rotating natural frequency at 411.36 Hz that, as shown in Fig. 3, corresponds to a wheel mode with two nodal diameters, and also for the various modes with 0 nodal diameters. This is a consequence of the instrumentation adopted in this work (according to the proposal presented in [26]), which cancels the response of the even harmonics and the contribution of these modes to the measured signal.

5. Conclusions

A global formulation for the equation of motion of a rotating railway wheelset through axisymmetric coordinates has been developed. The modelling is initially based on a rotating reference system from which the Lagrangian representation of the wheelset vibratory dynamics is obtained. Next, by employing a coordinate transformation to Eulerian coordinates, the corresponding equation of motion is derived with respect to a non-rotating coordinate frame. From either of these formulations, the corresponding free-response frequencies at which the rotating solid vibrates are calculated: they are the frequencies seen from a system that rotates

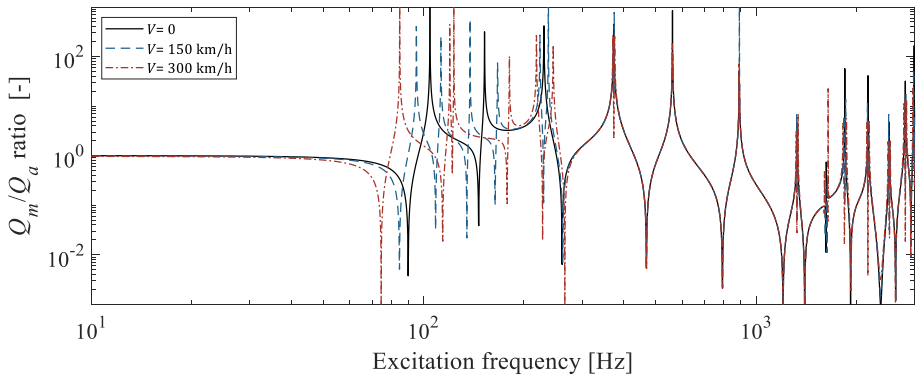

Fig. 10. Ratio between amplitudes of the measured (Q_m) and actual (Q_a) forces as function of the excitation frequency at three vehicle speeds.

with the wheelset (from the Lagrangian approach), or the frequencies observed from a non-rotating system (from the Eulerian one, corresponding to the forward and backward waves). A formula is proposed for calculating the natural frequencies in fixed axes as a function of the frequencies in rotating axes and the wheelset angular velocity.

The analysis of the natural frequencies in a rotating frame ω_L shows a generally small influence of the angular velocity. According to Eqs. (25) and (26), the dependence of the angular velocity Ω is produced through matrices **B** and **G**. The equation of motion term where **B** appears contains centripetal forces, while the term in which the matrix **G** appears corresponds to the Coriolis forces. Both effects can be considered as inertial effects associated with the wheelset rotation. When the vibration of a mode is observed from a fixed reference frame, the frequency ω_E corresponds to $\omega_E = \omega_L \pm h\Omega$, where h is the number of nodal diameters. The term $h\Omega$ corrects for the observer's point of view, and does not introduce any inertial effect. Consequently, the moving load models (formula given by $\omega_E = \omega_0 \pm h\Omega$, where ω_0 is the non-rotating frequency) are accurate only when the inertial effects associated with the rotation in a given mode are negligible.

The model is applied to a case with practical utility to study the response that is measured by the strain gauges used in instrumented wheelsets. This has been calculated by means of the Lagrangian formulation. Adopting a commonly used strain gauge configuration that compensates for temperature and centrifugal effects, the response to a constant vertical force acting in the wheel-rail contact is shown to be practically independent of the angular velocity. Nevertheless, in the case with a sinusoidal variation of the wheel-rail contact force with frequency ω, the wheelset responds at several frequencies that are multiples of the angular velocity above and below the frequency of the external force (that is $\omega \pm h\Omega$). This effect notably complicates the development of precise instrumented wheelsets able to measure at high frequencies as any compensation applied would have to be speed-dependent.

Declaration of Competing Interest

The authors declare that they have no known competing financial interests or personal relationships that could have appeared to influence the work reported in this paper.

Data availability

The authors are unable or have chosen not to specify which data has been used.

Acknowledgments

The first and second authors acknowledge the financial support through the grants PID2020-118013RB-C21 (funded by MCIN/AEI/10.13039/501100011033) and PROMETEO/2021/046 (funded by Generalitat Valenciana). The first author is very grateful to Dr Giacomo Squicciarini from the ISVR for the helpful discussions that contributed to increase the importance of the present work.

References

[1] X. Sheng, G. Cheng, D. Thompson, Modelling wheel/rail rolling noise for a high-speed train running along an infinitely long periodic slab track, Journal of the Acoustical Society of America 148 (1) (2020) 174–190, https://doi.org/10.1121/10.0001566.
[2] G. Cheng, Y. He, J. Han, X. Sheng, and D. Thompson, An investigation into the effects of modelling assumptions on sound power radiated froma high-speed train wheelset, Journal of Sound and Vibration, Article vol. 495, 2021, Art no. 115910, 10.1016/j.jsv.2020.115910.
[3] G. Tao, Z. Wen, X. Jin, X. Yang, Polygonisation of railway wheels: a critical review, Railway Engineering Science, Review 28 (4) (2020) 317–345, https://doi.org/10.1007/s40534-020-00222-x.
[4] B. Peng, S. Iwnicki, P. Shackleton, D. Crosbee, and Y. Zhao, The influence of wheelset flexibility on polygonal wear of locomotive wheels, Wear, Article vol. 432-433, 2019, Art no. 102917, 10.1016/j.wear.2019.05.032.
[5] Y. Ye, D. Shi, P. Krause, Q. Tian, M. Hecht, Wheel flat can cause or exacerbate wheel polygonization, Vehicle System Dynamics 58 (10) (2020) 1575–1604, https://doi.org/10.1080/00423114.2019.1636098.

[6] P. Vila, L. Baeza, J. Martínez-Casas, J. Carballeira, Rail corrugation growth accounting for the flexibility and rotation of the wheel set and the non-Hertzian and non-steady-state effects at contact patch, Vehicle System Dynamics, Conference Paper 52 (SUPPL. 1) (2014) 92–108, https://doi.org/10.1080/00423114.2014.881513.
[7] S. Zhang, G. Cheng, X. Sheng, D.J. Thompson, Dynamic wheel-rail interaction at high speed based on time-domain moving Green's functions, J. Sound Vib. 488 (2020/12/08/ 2020,), 115632, https://doi.org/10.1016/j.jsv.2020.115632.
[8] J. Fayos, L. Baeza, F.D. Denia, J.E. Tarancón, An Eulerian coordinate-based method for analysing the structural vibrations of a solid of revolution rotating about its main axis, Journal of Sound and Vibration 306 (3–5) (2007) 618–635, https://doi.org/10.1016/j.jsv.2007.05.051.
[9] J. Martínez-Casas, L. Mazzola, L. Baeza, S. Bruni, Numerical estimation of stresses in railway axles using a train–track interaction model, Int. J. Fatigue 47 (2013) 18–30, https://doi.org/10.1016/j.ijfatigue.2012.07.006.
[10] A. Guiral, A. Alonso, J.G. Giménez, Vehicle-track interaction at high frequencies - modelling of a flexible rotating wheelset in non-inertial reference frames, Journal of Sound and Vibration 355 (2015) 284–304, https://doi.org/10.1016/j.jsv.2015.06.032.
[11] J. Martínez-Casas, E. Di Gialleonardo, S. Bruni, L. Baeza, A comprehensive model of the railway wheelset-track interaction in curves, Journal of Sound and Vibration 333 (18) (2014) 4152–4169, https://doi.org/10.1016/j.jsv.2014.03.032.
[12] D.J. Thompson, Wheel-rail noise generation, part II: wheel vibration, Journal of Sound and Vibration 161 (3) (1993) 401–419, https://doi.org/10.1006/jsvi.1993.1083.
[13] D.J. Thompson, Wheel-rail noise generation, part V: inclusion of wheel rotation, Journal of Sound and Vibration 161 (3) (1993) 467–482, https://doi.org/10.1006/jsvi.1993.1086.
[14] M. Geradin, N. Kill, A new approach to finite element modelling of flexible rotors, Eng. Comput. 1 (1) (1984) 52–64, https://doi.org/10.1108/eb023560.
[15] R.W. Stephenson, K.E. Rouch, R. Arora, Modelling of rotors with axisymmetric solid harmonic elements, J. Sound Vib. 131 (3) (1989) 431–443.
[16] L. Hu, A. Palazzolo, An Enhanced Axisymmetric Solid Element for Rotor Dynamic Model Improvement, ASME Journal of Vibration and Acoustics 141 (5) (2019), 051002, https://doi.org/10.1115/1.4043411.
[17] F. Treyssède, J. Cesbron, Waveguide finite element modelling for broadband vibration analysis of rotating and prestressed circular structures: application to tyres, J. Sound Vib. 543 (2022), 117361, https://doi.org/10.1016/j.jsv.2022.117361.
[18] X. Sheng, Y. Liu, X. Zhou, The response of a high-speed train wheel to a harmonic wheel-rail force, J. Phys. Conf. Ser. 744 (2016) 012145.
[19] L. Baeza, J. Giner-Navarro, D.J. Thompson, J. Monterde, Eulerian models of the rotating flexible wheelset for high frequency railway dynamics, Journal of Sound and Vibration 449 (2019) 300–314, https://doi.org/10.1016/j.jsv.2019.03.002.
[20] UIC 518-2009 Testing and Approval of Railway Vehicles from the Point of View of Their Dynamic Behaviour-Safety-Track Fatigue-Running Behaviour, Testing and Approval of Railway Vehicles from the Point of View of Their Dynamic Behaviour - Safety - Track Fatigue - Running Behaviour, 2009.
[21] H. Wu, N. Wilson, in: Handbook of Railway Vehicle Dynamics, CRC Press, 2006, pp. 209–237.
[22] P. Gullers, L. Andersson, R. Lundén, High-frequency vertical wheel-rail contact forces-field measurements and influence of track irregularities, Wear, Article 265 (9–10) (2008) 1472–1478, https://doi.org/10.1016/j.wear.2008.02.035.
[23] J.C.O. Nielsen, High-frequency vertical wheel-rail contact forces-Validation of a prediction model by field testing, Wear 265 (9–10) (2008) 1465–1471, https://doi.org/10.1016/j.wear.2008.02.038.
[24] M. Petyt, Introduction to finite element vibration analysis, Second Edition, Chapter 5 (2010) 148–191.
[25] M.I. Friswell, J.E.T. Penny, S.D. Garvey, A.W. Lees (Eds.), Dynamics of Rotating Machines, Cambridge University Press, 2010.
[26] E. Gomez, J.G. Giménez, A. Alonso, Method for the reduction of measurement errors associated to the wheel rotation in railway dynamometric wheelsets, Mech. Syst. Sig. Process. 25 (8) (2011) 3062–3077.